https://dx.doi.org/10.1016/j.compositesb.2022.110074

Magnolol-derived thiol-ene photo-polymerized membranes with intrinsic anti-flammability and high transparency

Wenwen Guo [a, b, c, *], Fuwei Liang [a], Shun Chen [a], Kejing Yu [a], Jie Sun [a], Zengyuan Pang [a], Bin Fei [b, *]

[a] Key Laboratory of Eco-textiles, Ministry of Education, College of Textile Science and Engineering, Jiangnan University, 1800 Lihu Avenue, Wuxi, Jiangsu 214122, China.

[b] Institute of Textiles and Clothing, The Hong Kong Polytechnic University, Hong Kong, China.

[c] State Key Laboratory of Fire Science, University of Science and Technology of China, 96 Jinzhai Road, Hefei, Anhui 230026, China.

*Corresponding Author: Wenwen Guo, Bin Fei. Email: guoww@jiangnan.edu.cn (W. Guo), bin.fei@polyu.edu.hk (B. Fei).

Abstract

In this study, a phosphorus-containing bio-based monomer (MBDPP) was first synthesized from renewable magnolol, and subsequently photo-cured with tri-thiol (TPTMP) or tetra-thiol (PETMP) monomers via thiol–ene polymerization. The synthesized MBDPP/TPTMP and MBDPP/PETMP membranes exhibited high char residues at 700 °C in the TGA tests, which were 19.8 wt% and 24.2 wt% for nitrogen while 16.5 wt% and 20.2 wt% for air, respectively, indicating superior charring capacity of both membranes. DMA results indicated that both the higher stiffness and the T_g of the cured MBDPP/PETMP membrane was ascribed to its higher cross-linking density

than that of the cured MBDPP/TPTMP owing to the tetra-functional groups of PETMP. In the open flame test, both MBDPP/TPTMP and MBDPP/PETMP membranes self-extinguished immediately when removing the flame source, manifesting excellent intrinsic anti-flammability. The cone calorimeter results further demonstrated that MBDPP/TPTMP and MBDPP/PETMP membranes showed lower PHRR (419 and 388 kW/m^2, respectively) and THR (41.38 and 38.98 MJ/m^2, respectively) values than most of the thiol-ene photo-polymerized counterparts previously reported. The excellent anti-flammability of MBDPP/TPTMP and MBDPP/PETMP membranes originated from the formation of expandable char residues that played an efficient role in hampering the transfer of flammable pyrolysis products to flame zone as well as insulating the heat irradiation during combustion. Additionally, both MBDPP/TPTMP and MBDPP/PETMP membranes showed excellent transparency (transmittance > 85% in the visible region) and flexibility (breaking elongation around 40%). Taking the intrinsic anti-flammability, exceptional transparency and high flexibility into account, the MBDPP/TPTMP and MBDPP/PETMP systems are suitable as intumescent flame retardant coating materials.

Keywords: Magnolol; Thiol-ene photo-polymerization; Anti-flammability; Transparency

1. Introduction

UV photo-polymerization technology is well known as an eco-friendly technology, which has been widely applied in diverse fields, such as coatings, adhesives, photosensitive materials, photoresists and 3D printing [1-5]. Thiol-ene photo-

polymerized systems have attracted the extensive attention because of their advantages such as rapid curing and low shrinkage [6]. In addition, the presence of thiol group can effectively solve the problem of oxygen polymerization inhibition of acrylate system [7]. However, like conventional UV curable resins (such as epoxy acrylate and polyurethane acrylate), thiol-ene photo-polymerized systems are also highly flammable and cannot be used in some occasions with high flame retardant requirements. Therefore, there is an urgent demand for simple and effective methods to solve the flammability of these UV curable coatings, which is of great significance to further expand their applications.

Generally, an effective way to reduce the flammability of UV curing coating is to chemically bond the flame retardant monomers/oligomers to the polymer main chain, that is, to use UV curable flame retardant monomers/oligomers. Liu *et al.* synthesized two phosphorus-containing diene and a nitrogen-containing trithiol monomers, and cured them by thiol–ene photo-polymerization [8]. The resultant cured coating showed enhanced anti-flammability owing to the co-addition of phosphorous and nitrogen. Çakmakçı et al. prepared a boron-containing thiol–ene polymerized coating, and the cured coating had an increased LOI to 24.2% when the boron content was 1.44% [9]. Çakmakçı et al. also synthesized an allyldiphenyl phosphine oxide (ADPPO) based UV cured coating by thiol–ene polymerization [10]. The LOI values of the cured coatings increased with the increase of ADPPO dosage. Specifically, the highest LOI value was 27.5% when the ADPPO dosage was 35 wt% (phosphorus content: 4.4%). Baştürk *et al.* synthesized a phosphorous-containing monomer, bis-(triethoxysilylpropyl) phenyl

phosphamide (BESPPA), and further fabricated a hybrid coating by virtue of thiol–ene polymerization of BESPPA [11]. The LOI of the UV cured hybrid coating was increased to 26.5% owing to the phosphorus–silicon synergism. However, the preparation of UV curable flame retardant monomers/oligomers aforementioned are derived from petroleum-based resources, and no renewable resources are involved.

With the increasing awareness of sustainable development, flame retardant monomers/oligomers begin to turn to bio-based mass in recent years. Guo's group prepared a photo-cured coating via thiol–ene polymerization of castor oil based thiol and phosphorus- and silicon-containing monomers [12]. By adjusting the ratio between the components, the UV cured coating behaved excellent anti-flammability, achieving an LOI of 27.6% and UL-94 V-0 grade. In another study, Guo's group deposited the above photo-cured coating onto the wood surface [13]. The average heat release rate and the total heat release of the coated wood were 74% and 73% lower than those of the uncoated one. These studies convince us that the flame retardant modification of bio-based mass is an effective approach to prepare anti-flammable UV curable monomers.

Magnolol is bio-based compound that derives from natural plants Magnolia officinalis. Magnolol has two allyl groups in its molecular structure, which is a suitable candidate as UV curable monomer. Additionally, magnolol also has two phenolic hydroxyl groups, which facilities its modification by flame retardants. In this study, we first synthesized a phosphorus-containing magnolol-based monomer (MBDPP), and subsequently cured MBDPP with tri-thiol or tetra-thiol monomers by thiol–ene

polymerization. The thermal stability, flame retardancy, transparency, and tensile property of the cured membranes were investigated. Finally, the flame retardant mode of action was further clarified for these bio-based thiol-ene photo-polymerized networks.

2. Experimental

2.1. Materials

Magnolol, diphenyl phosphoryl chloride (DPPC), anhydrous sodium sulfate, trimethylolpropane tris(3-mercaptopropionate) (TPTMP), pentaerythritol tetra(3-mercaptopropionate) (PETMP), and 2, 2-dimethoxy-2-phenylacetophenone (DMPA) were purchased from Aladdin Chemical, China. Triethylamine and dichloromethane were provided by the Sinopharm Chemical Reagent Co., Ltd., China. All the reagents were used as received.

2.2. Synthesis of magnolol-derived bis(diphenyl phosphate) (MBDPP)

In a 500 mL three-neck flask equipped with a mechanical stirrer and a nitrogen inlet, magnolol (25.0 g, 0.0939 mol) and triethylamine (19.00 g, 0.188 mol) were dissolved in dichloromethane (100 mL). Then, DPPC (50.50 g, 0.188 mol) dissolved in 50 mL of dichloromethane was added dropwise into the flask over a period of 1 h at 0 °C. The reaction system was kept at 0 °C for 3 h and 50 °C for another 3 h. After completion of the reaction, the mixture was filtered to remove the precipitate, and then the filtrate was poured into the separatory funnel and washed with distilled water several times. After that, the organic layer was separated and dried with anhydrous sodium sulfate overnight. The solvent was removed under vacuum by a rotary evaporator, and the yellow viscous

liquid was obtained and dried at 60 °C for 24 h for further use. The synthetic route of MBDPP was shown in scheme 1a.

2.3. Fabrication of polymer films by photo-polymerization

Scheme 1b and 1c illustrates the chemical structures of thiol-monomers (TPTMP and PETMP) and photo-initiator DMPA, and the preparation of polymer films by photo-polymerization. For the preparation of MBDPP/TPTMP polymer film, MBDPP (17.54 g, 24 mmol), TPTMP (6.38 g, 16 mmol) and DMPA (0.48 g) (2 wt% to the total weight) were mixed at ambient temperature under stirring for 15 min in a beaker. Then, the obtained homogeneous mixture was poured to a plastic mold with a thickness approximately 3 mm. The mixture was photo-polymerized by a high-pressure mercury lamp (500 W) for 10 min, and the distance between the lamp and the mixture was 35 cm. The MBDPP/PETMP polymer film was prepared using a similar method just replacing TPTMP by PETMP (Allyl mole was equal to thiol one).

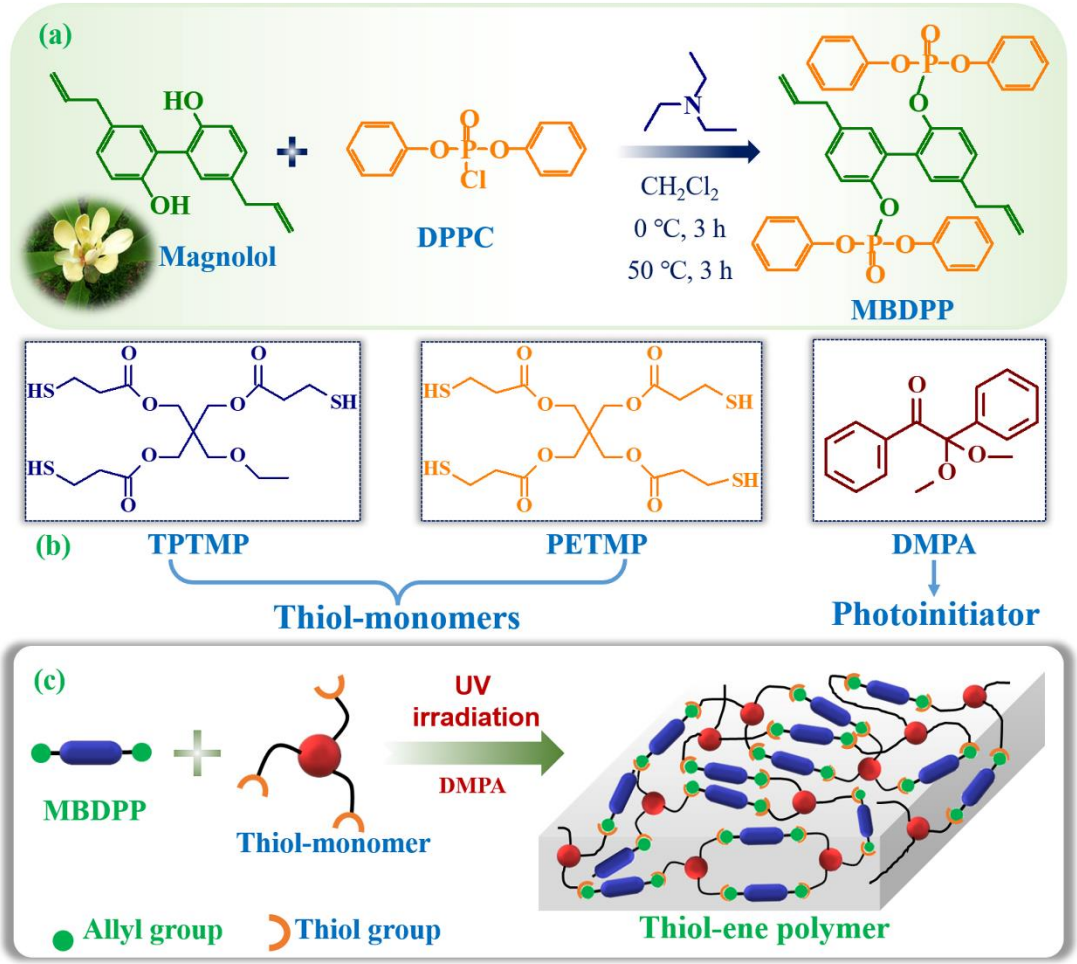

Scheme 1. (a) Synthetic route of MBDPP; (b) chemical structures of thiol-monomers and DMPA; (c) preparation of thiol-ene polymer films by photo-polymerization

2.4. Characterization

The detail information about the methods and instruments was given in the supporting information.

3. Results and discussion

3.1. Structural characterization of MBDPP

Magnolol-derived bis(diphenyl phosphate) (MBDPP) was synthesized from the dehydrochlorination reaction between magnolol and DPPC. The molecular structure of MBDPP was confirmed using the NMR spectrometer. As shown in Fig. 1a, the proton

NMR spectrum of DPPC displayed multiple signals in the range of 7.20-7.40 ppm were attributed to the protons of the aromatic rings. After the substitution reaction with magnolol, except for the analogous multiple signals of aromatic rings, several new peaks can be observed from the proton NMR spectrum of MBDPP (Fig. 1b), the signals at around 3.45 ppm were assigned to the hydrogen atoms of the methylene group (marked by a) adjacent to the C=C double bond. The signals at around 5.98 and 5.10 ppm were allocated to the hydrogen atoms of the C=C double bond (marked by b and c). All these proton signals match well with the designed molecular structure of MBDPP. Furthermore, Fig. 1c provided the phosphorus NMR spectrum of DPPC, which exhibited a single peak located at approximately -5.20 ppm. Correspondingly, the phosphorus NMR spectrum of MBDPP (Fig. 1d) also displayed a single intense signal at -17.08 ppm, which accorded well with the single chemical surrounding of phosphorus atom in the MBDPP structure. Moreover, the movement of the single peak position demonstrated the successful reaction between DPPC and magnolol. Additionally, in the ^{13}C NMR spectrum of MBDPP (Fig. 1e), the chemical shift of all the signals was in good agreement with the expected structure.

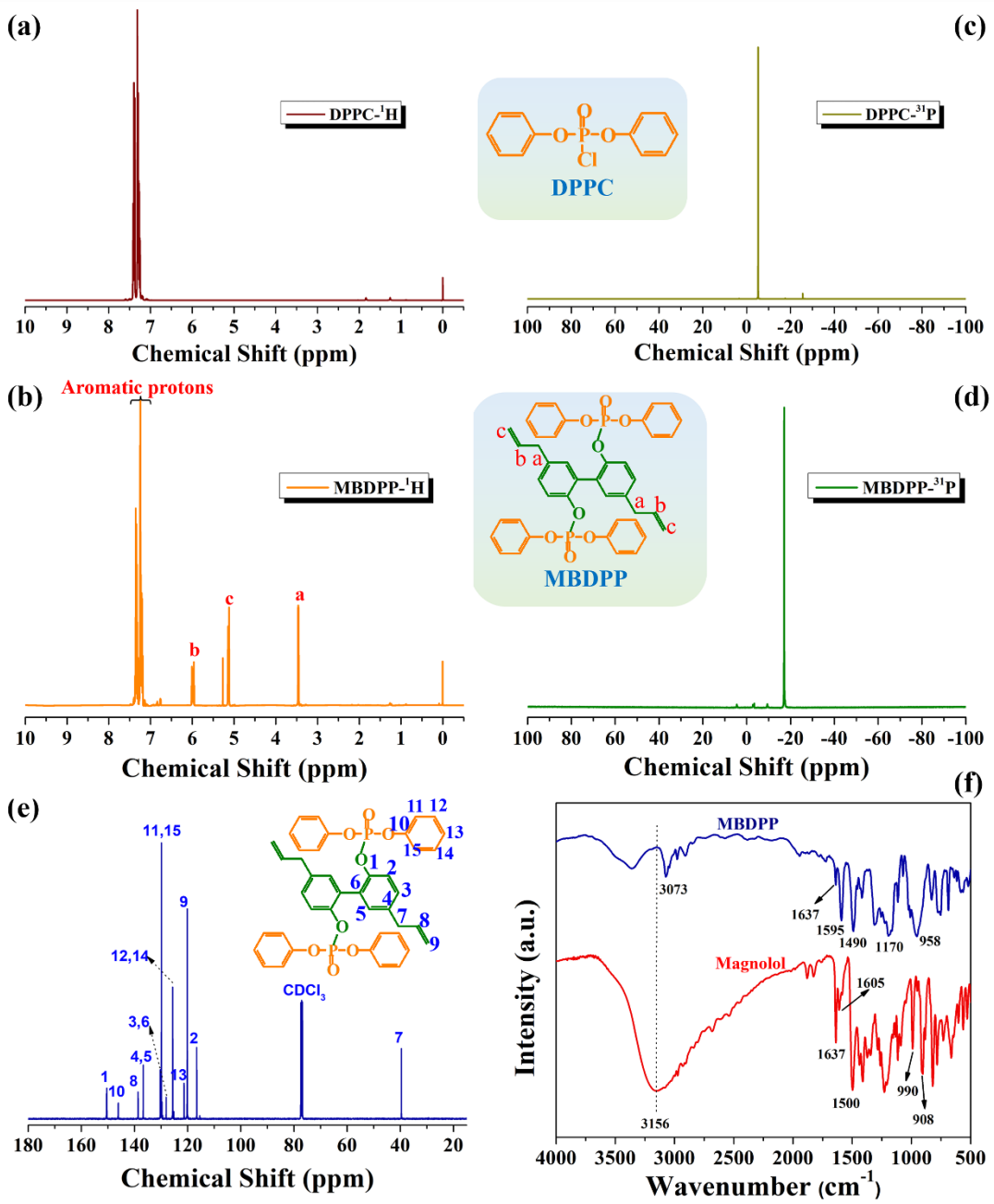

Fig. 1. The Hydrogen bond complexasionproton and phosphorus NMR spectra of (a, c) DPPC and (b, d) MBDPP; (e) the carbon NMR spectra of MBDPP; (f) FTIR spectra of magnolol and MBDPP

Fig. 1f compares the FTIR spectra of magnolol and MBDPP. For magnolol, the characteristic bands at 1637, 990 and 908 cm^{-1} were ascribed to the vibrations of the double bond in the allyl group [14]. The characteristic bands at 1605 and 1500 cm^{-1}

were corresponding to the skeleton vibration of the aromatic rings. Additionally, the broad and intense band at around 3156 cm^{-1} belonged to the stretching vibration of the phenolic hydroxyl groups. For MBDPP, the absence of the broad and intense band corresponding to the phenolic hydroxyl groups of magnolol implied the occurrence of the dehydrochlorination reaction between magnolol and DPPC. The skeleton vibration of the aromatic rings also shifted to 1595 and 1490 cm^{-1}, owing to the substitution of diphenyl phosphate. Several new bands at 1170 cm^{-1} (P=O) [15] and 958 cm^{-1} (P-O-Ph) [14] appeared, which further manifested the successful substitution of diphenyl phosphate.

3.2. Photo-polymerization kinetics

MBDPP/TPTMP and MBDPP/PETMP membranes were synthesized via thiol-ene photo-polymerization. Thus, FTIR spectra were employed to monitor the change of thiol (2565 cm^{-1}) and allyl (1638 cm^{-1}) groups in the systems in order to clarify the photo-polymerization kinetics. Fig. 2a and 2b illustrates the changes of FTIR spectra of MBDPP/TPTMP and MBDPP/PETMP systems under different UV irradiation time. The changes of transmittance intensity of allyl groups (1638 cm^{-1}) and thiol groups (2565 cm^{-1}) are further depicted in Fig. 2c and 2d for MBDPP/TPTMP and Fig. 2e and 2f for MBDPP/PETMP. It can be intuitively observed that the transmittance intensity of thiol and allyl groups decreased gradually with the increase of the UV irradiation time for both MBDPP/TPTMP and MBDPP/PETMP films, indicating the photo-polymerization reaction occurs between MBDPP and thiol-monomers. The conversion rate was computed by the change of the transmittance peak. Fig. 2g and 2h give the

conversion rate of thiol and allyl groups against UV irradiation time, respectively. The conversion rate of both thiol and allyl groups increased rapidly at the beginning and then reach equilibrium after 120 s. With the extension of UV irradiation time, the conversion rate showed very slight change and was lower than 100% eventually. Additionally, the conversion rate of allyl group was slightly higher than that of thiol group for both MBDPP/TPTMP and MBDPP/PETMP systems, owing to the homo-polymerization capacity of allyl group [16]. Finally, the conversion rate of thiol and allyl groups achieved >75% for both systems, manifesting the occurrence of the efficient photo-polymerization.

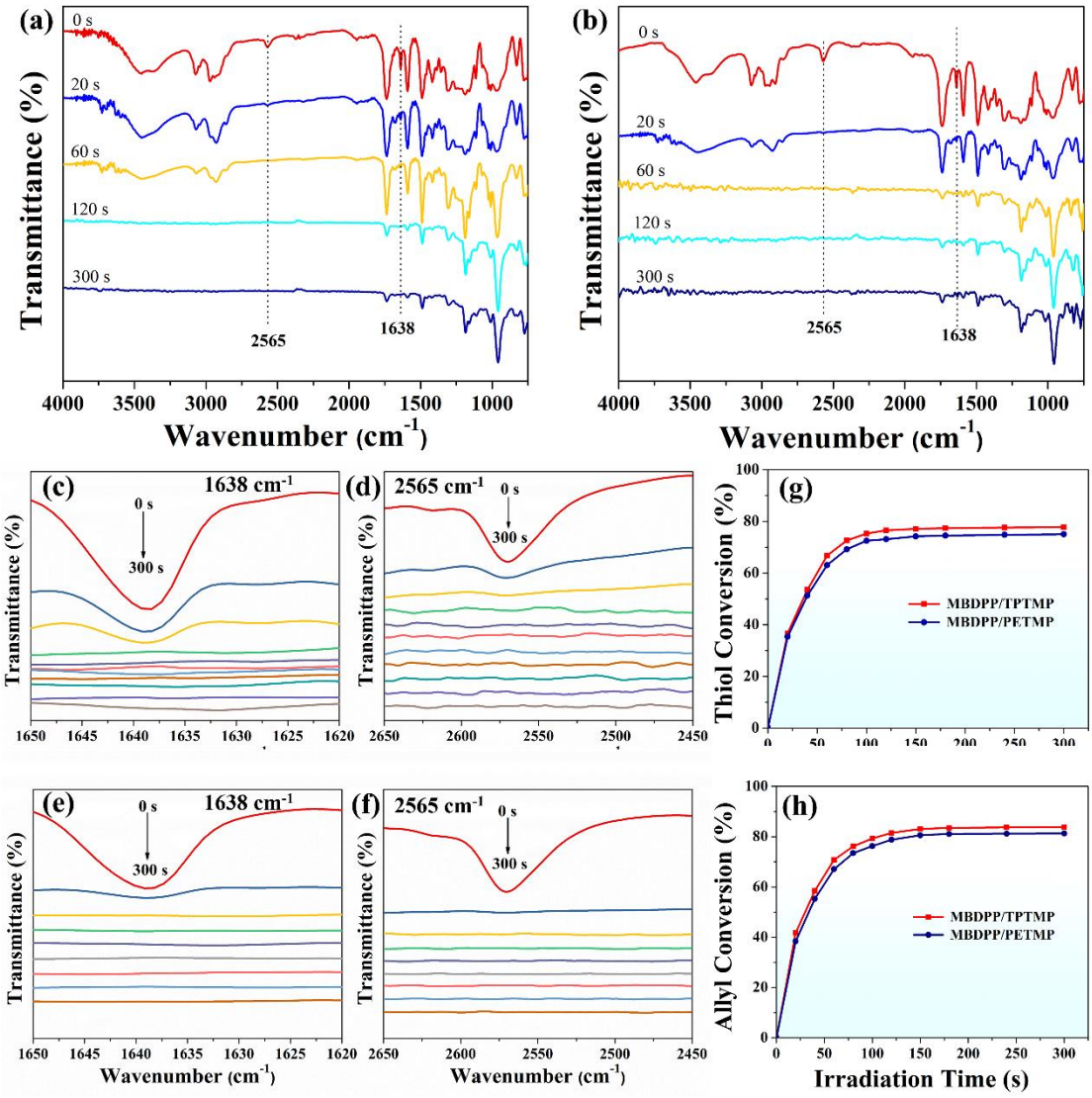

Fig. 2. The changes of FTIR spectra of (a) MBDPP/TPTMP and (b) MBDPP/PETMP systems with irradiation time; the partial enlarged view of FTIR spectra of allyl (1638 cm^{-1}) and thiol (2565 cm^{-1}) groups for (c, d) MBDPP/TPTMP and (e, f) MBDPP/PETMP; conversion of (g) thiol and (h) allyl groups against UV irradiation time.

3.3. Thermal decomposition behaviors

Fig. 3 depicts the TGA and differential TGA (DTG) profiles of MBDPP/TPTMP and MBDPP/PETMP membranes in nitrogen and air atmospheres, several typical data including the temperatures at 5 wt% mass loss (T_d), the temperatures at 50 wt% mass

loss ($T_{-50\%}$), the temperatures at the maximum weight loss rate (T_{max}) and the char residue (%) at 700 °C was summarized in Table 1. As shown in Fig. 3a and 3c, MBDPP/TPTMP membrane exhibited two decomposition stages in the temperature regions of 200-350 °C (31% mass loss) and 350-410 °C (39% mass loss) under nitrogen. Similarly, MBDPP/PETMP membrane also decomposed in two stages in the temperature regions of 200-350 °C (34% mass loss) and 350-410 °C (33% mass loss). The first decomposition stage was corresponding to the cleavage of thermally instable P-O-C bond and release of phosphate species, while the second one was associated with the split of polymer networks promoted by phosphate species. It can be observed from Table 1 that the typical temperatures including T_d, $T_{-50\%}$ and T_{max} values of MBDPP/TPTMP and MBDPP/PETMP membranes under nitrogen was very close, implying similar thermal stability under nitrogen. Additionally, the char residues of MBDPP/TPTMP and MBDPP/PETMP membranes at the end of decomposition were about 19.8 wt% and 24.2 wt%, respectively. The higher char residue of MBDPP/PETMP membrane over MBDPP/TPTMP was ascribed to the higher cross-linking density of the former, since the higher cross-linking density was conducive to proceeding carbonization. In addition, the estimated LOI values of MBDPP/TPTMP and MBDPP/PETMP membranes were 25.4% and 27.2%, respectively, indicating better anti-burning properties for both of two membranes. Moreover, different from nitrogen atmosphere (Fig. 3b and 3d), MBDPP/TPTMP membrane underwent three decomposition stages in the temperature regions of 200-350 °C (33% mass loss), 350-400 °C (30% mass loss) and 400-700 °C (21% mass loss) under air. Similarly,

MBDPP/PETMP membrane also displayed three stages in the temperature regions of 200-350 °C (33% mass loss), 350-400 °C (30% mass loss) and 400-700 °C (17% mass loss). The former two stages were attributed to the cleavage of phosphate groups and backbones of polymer networks, respectively, whereas the third one was related to the slowly thermal oxidation of the residues. Similar to the results under nitrogen, the thermal performance parameters including T_d, $T_{-50\%}$ and T_{max} values of MBDPP/TPTMP were also very close with those of MBDPP/PETMP membranes under air, indicating alike thermal-oxidative degradation processes of MBDPP/TPTMP and MBDPP/PETMP membranes. With proceeding decomposition, MBDPP/TPTMP and MBDPP/PETMP membranes showed 19.8 wt% and 24.2 wt% residue at 700 °C, respectively, demonstrating good charring capacity.

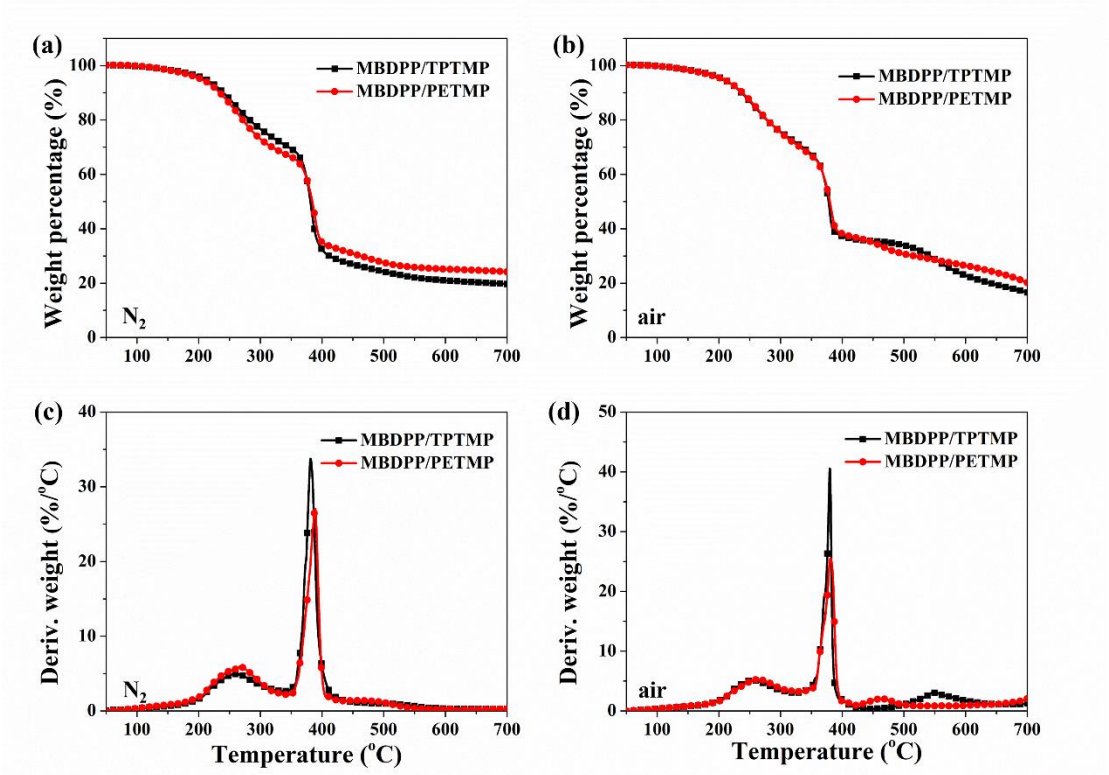

Fig. 3. TGA and differential TGA (DTG) profiles of MBDPP/TPTMP and MBDPP/PETMP membranes in (a, c) nitrogen and (b, d) air atmospheres

Table 1. Thermogravimetric data of MBDPP/TPTMP and MBDPP/PETMP membranes in nitrogen and air atmospheres

Sample	T_d (°C)		$T_{-50\%}$ (°C)		T_{max} (°C)		Char residue (%) [a]		Estimated LOI (%) [b]
	N_2	Air	N_2	Air	N_2	Air	N_2	Air	
MBDPP/TPTMP	211	207	381	378	381	380	19.8	19.8	25.4
MBDPP/PETMP	204	206	384	380	389	381	24.2	24.2	27.2

Notes:

[a] Measured at 700 °C.

[b] Calculated using the equation LOI = 17.5 + 0.4(CY) [17, 18]

3.4. Thermo-mechanical properties

The thermo-mechanical properties of MBDPP/TPTMP and MBDPP/PETMP membranes were investigated by the dynamic mechanical analysis. Fig. 4a and 4b depicts the storage modulus (E') and the tanδ against temperature curves of MBDPP/TPTMP and MBDPP/PETMP membranes, and Table 2 summarizes the typical parameters. The storage modulus (E') curves of both MBDPP/TPTMP and MBDPP/PETMP membranes showed a sharp drop from glassy state to rubbery state. The E' of MBDPP/PETMP membrane was higher than that of MBDPP/TPTMP in the glassy state, indicating the higher stiffness of MBDPP/PETMP membrane. The glass transition temperature (T_g) is a crucial parameter that denotes the transition from glassy state to rubbery state, corresponding to the temperature at the peak of the tanδ curves. The T_g of MBDPP/TPTMP and MBDPP/PETMP membranes was 7 °C and 13 °C,

respectively. Both the T_g values were lower than 20 °C, indicating the flexibility of both the membranes at the room temperature. Both the higher stiffness and the T_g of MBDPP/PETMP membrane was ascribed to its higher cross-linking density than that of MBDPP/TPTMP owing to the tetra-functional groups of PETMP. In order to verify this viewpoint, the cross-linking density (υ_e) was calculated using the formula as below [19, 20]:

$$\upsilon_e = E'/3RT$$

where E', R and T represent the storage modulus at T_g+30 ºC, the gas constant (8.314 J/(mol·K)), and the absolute temperature of T_g+30 ºC, respectively. The υ_e values were 111 and 184 mol/m^3 for MBDPP/TPTMP and MBDPP/PETMP membranes, respectively, following the same trend as that of T_g. The DMA results demonstrated that the cross-linking density was dependent upon the functionality of monomers, further affecting the E' and T_g.

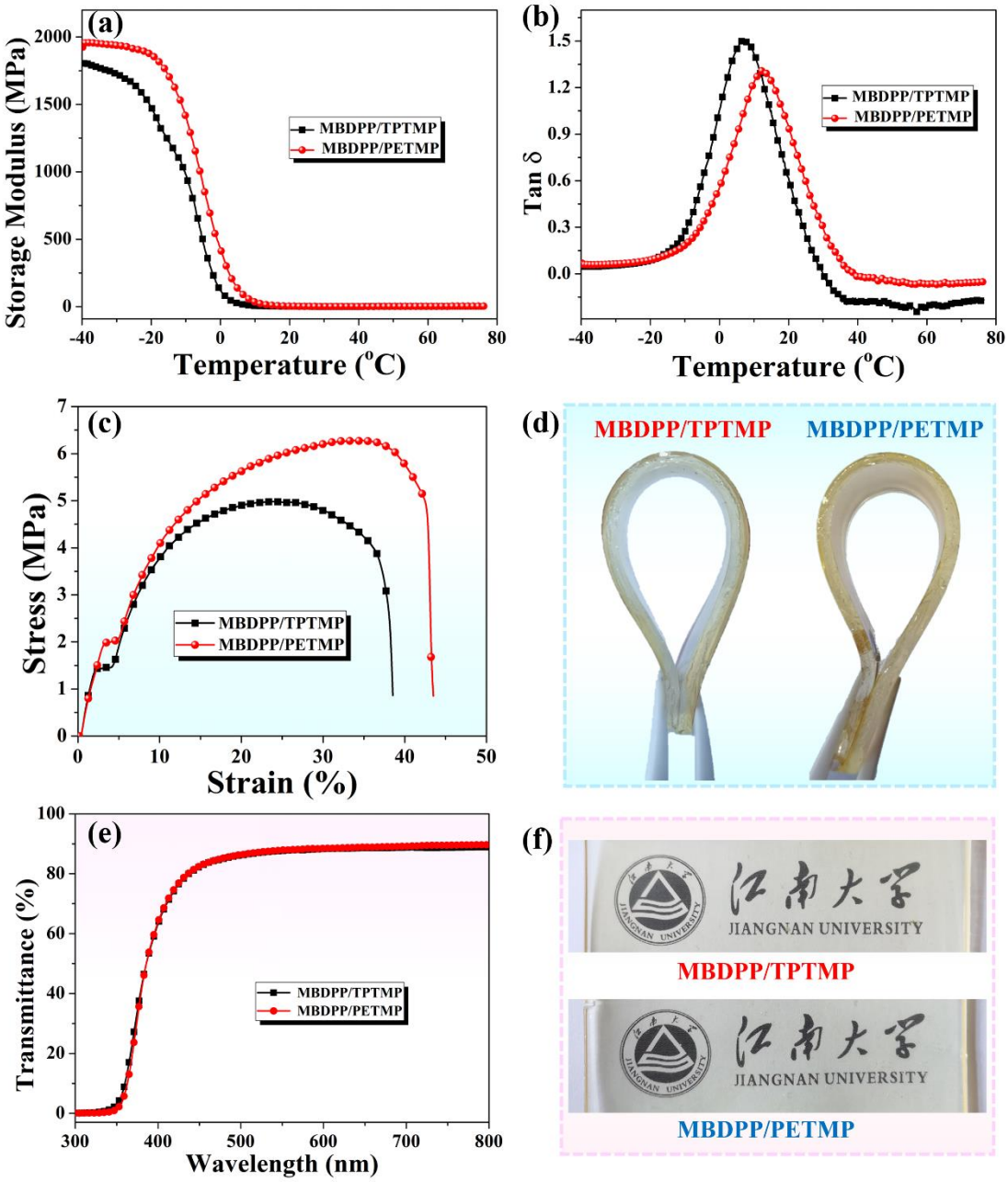

Fig. 4. (a) The storage modulus (E') and (b) the tanδ against temperature curves of MBDPP/TPTMP and MBDPP/PETMP membranes; (c) the tensile stress-strain profiles and (d) flexibility photographs of MBDPP/TPTMP and MBDPP/PETMP membranes (3mm); (e) the UV–Vis spectra and (f) transparency photographs of MBDPP/TPTMP and MBDPP/PETMP membranes (3.0 mm).

Table 2. Thermo-mechanical parameters of MBDPP/TPTMP and MBDPP/PETMP membranes

Samples	T_g (°C)	E' at -40 °C (MPa)	E' at T_g+30 °C (MPa)	υ_e (mol/m^3)
MBDPP/TPTMP	7	1803	0.86	111
MBDPP/PETMP	13	1949	1.45	184

3.7. Tensile properties

Fig. 4c gives the tensile stress-strain profiles of MBDPP/TPTMP and MBDPP/PETMP membranes. Both the MBDPP/TPTMP and MBDPP/PETMP membranes exhibited typical stress-strain profiles with yield behaviors. Specifically, MBDPP/TPTMP membrane showed a tensile strength of 4.98 MPa and an elongation at break of 39%, while MBDPP/PETMP membrane displayed a tensile strength of 6.28 MPa and an elongation at break of 43%. The MBDPP/PETMP membrane had superior tensile strength over the MBDPP/TPTMP one, which could be ascribed to the higher cross-linking density of the former system. Additionally, the elongation at break of both the membranes was around 40%, suggesting the good flexibility of these membranes. In order to observe the flexibility of the membranes more intuitively, the digital photos of MBDPP/TPTMP and MBDPP/PETMP membranes was displayed in Fig. 4d, both the membranes presented great flexibility. Taking the low tensile strength and the high flexibility into account, the MBDPP/TPTMP and MBDPP/PETMP systems are suitable as intrinsic flame retardant coating materials.

3.8. Optical properties

UV–Vis spectroscopy was employed to evaluate the optical performance of the samples. Fig. 4e provides the UV–Vis spectra of MBDPP/TPTMP and MBDPP/PETMP membranes (3.0 mm). Both the membranes exhibited high transmittance (> 85%) beyond 500 nm, manifesting the good transparency in the visible region that was evidenced by the photographs in Fig. 4f. Both the membranes displayed almost zero transmittance in the ultraviolet region (< 350 nm), implying its potential application as UV protection membranes. MBDPP/TPTMP and MBDPP/PETMP membranes showed a very slight yellow color, which was probably caused by the degradation product of the photo-initiator [21].

3.5. Flame retardant properties

Flame retardant properties of MBDPP/TPTMP and MBDPP/PETMP membranes were assessed by the open flame test. Fig. 5 depicts the screenshots of MBDPP/TPTMP and MBDPP/PETMP membranes exposure to an alcohol burner. During the exposure to the open flame for 10 s twice, both MBDPP/TPTMP and MBDPP/PETMP membranes showed immediate self-extinction performance when removing the flame source, manifesting excellent intrinsic anti-flammability.

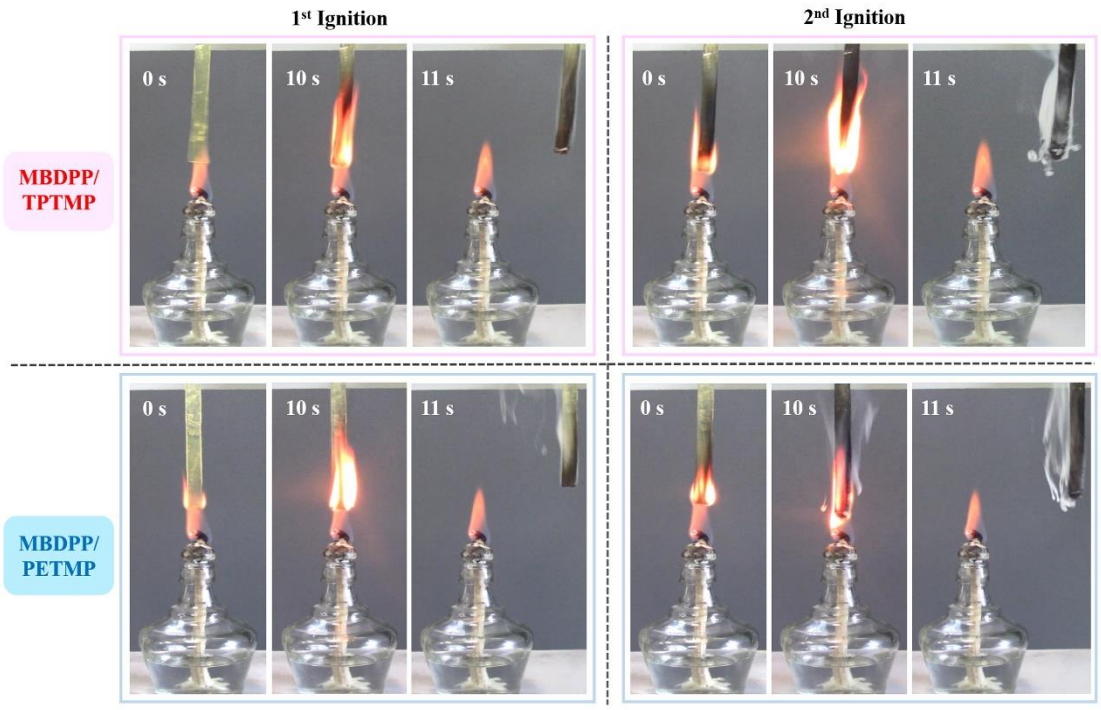

Fig. 5. Screenshots of MBDPP/TPTMP and MBDPP/PETMP membranes exposure to open flame

Cone calorimeter has been regarded as one of the most effective bench-scale apparatus to provide multiple flammability parameters [22-27]. Fig. 6a gives the heat release rate (HRR) versus time plots of MBDPP/TPTMP and MBDPP/PETMP membranes, and Table 3 summarizes the relating data. A single HRR peak was visible from 30 to 250 s for MBDPP/TPTMP and MBDPP/PETMP membranes, with the time to ignition (t_{ig}) value of 26 and 30 s, respectively. The MBDPP/TPTMP and MBDPP/PETMP membranes behaved the peak HRR (PHRR) value of 419 and 388 kW/m^2, respectively. The total heat release (THR) of MBDPP/TPTMP and MBDPP/PETMP membranes was 41.38 and 38.98 MJ/m^2, respectively (Fig. 6b). The PHRR and THR values of MBDPP/TPTMP and MBDPP/PETMP membranes were relatively lower than most of the photo-polymerized systems previously reported [14,

28-31] (Fig. 6c), demonstrating their effectively intrinsic anti-flammability. Additionally, the PHRR and THR values of MBDPP/PETMP were lower than those of MBDPP/TPTMP, which was attributed to the better carbonization ability induced by the higher crosslinking density. Furthermore, the high char residues of 21.4 wt% and 26.3 wt% were observed for MBDPP/TPTMP and MBDPP/PETMP, respectively (Fig. 6d), indicating the predominant mode of action in the condensed phase. As shown in Fig. 6e and 6f, both the MBDPP/TPTMP and MBDPP/PETMP membranes exhibited very similar total smoke production (TSP) and peak smoke production rate (SPR) values. Such low TSP and peak SPR values suggested the high fire safety characteristics of MBDPP/TPTMP and MBDPP/PETMP membranes, which was favorable to fire rescue and casualty reduction.

The pyrolysis combustion performances of MBDPP/TPTMP and MBDPP/PETMP membranes were further evaluated by MCC test[32, 33]. The heat release rate (HRR) curves of MBDPP/TPTMP and MBDPP/PETMP were shown in Fig. S1, and several key flammability parameters of the membranes including peak heat release rate (PHRR), total heat released (THR), and temperature at PHRR (T_p) were summarized in Table S1. as shown in Fig. S1, the pyrolysis HRR curves of MBDPP/TPTMP and MBDPP/PETMP presented similar shape and close THR and T_p values, except for that the PHRR value of MBDPP/PETMP (196.5 W/g) was lower than that of MBDPP/TPTMP (216.2 W/g), indicating better flame retardant performance of MBDPP/PETMP.

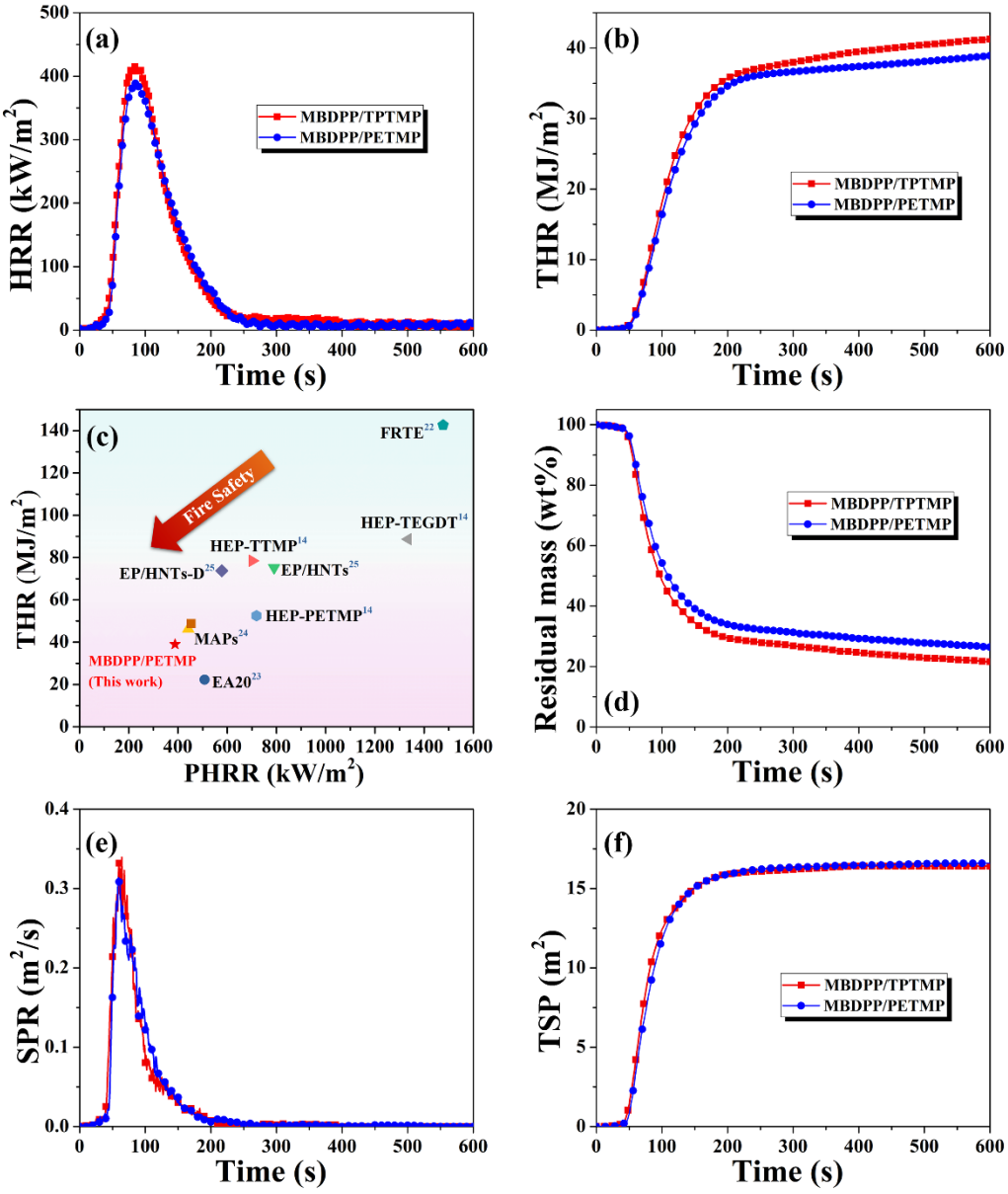

Fig. 6. (a) HRR and (b) THR against time plots of MBDPP/TPTMP and MBDPP/PETMP membranes; (c) Comparison of the PHRR and THR values of MBDPP/PETMP membrane with the previously reported values of the counterparts; (d) Mass loss, (e) TSP and (f) SPR against time plots of MBDPP/TPTMP and MBDPP/PETMP membranes.

Table 3. Cone calorimetric data of MBDPP/TPTMP and MBDPP/PETMP membranes

Samples	t_{ig} (s)	PHRR (kW/m^2)	THR (MJ/m^2)	TSP (m^2)	Peak SPR (m^2/s)	Residue (wt%)
MBDPP/TPTMP	26±1.8	419±18.9	41.38±1.4	16.42±0.48	0.33±0.02	21.4±0.7
MBDPP/PETMP	30±2.4	388±20.5	38.98±1.2	16.60±0.33	0.31±0.02	26.3±0.9

3.6. Flame retardant mechanism

The morphological features of the char residues could reflect the flame retardant mode of action in the condensed phase[34, 35]. Fig. 7 a and 7b depicts the photographs of the char residues of MBDPP/TPTMP and MBDPP/PETMP membranes after the cone calorimeter measurement. It can be found that both the MBDPP/TPTMP and MBDPP/PETMP membranes exhibited notably intumescent char residues. The original thickness of the membranes was about 3 mm, and the height of the char residues was more than 40 mm, implying more than 10 times of the expansion ratio. As is well known, the expandable char residues play an efficient role in hampering the transfer of flammable pyrolysis products to flame zone as well as insulating the heat irradiation. Under the SEM observation, the char residues of both the MBDPP/TPTMP and MBDPP/PETMP membranes showed an intact and dense surface, which further strengthened the barrier effect. Thus, it can be concluded that both the MBDPP/TPTMP and MBDPP/PETMP membranes are prone to form an intumescent structured char that functioned as a physical barrier for combustible products and heat transfer, and further

enhanced the flame retardancy.

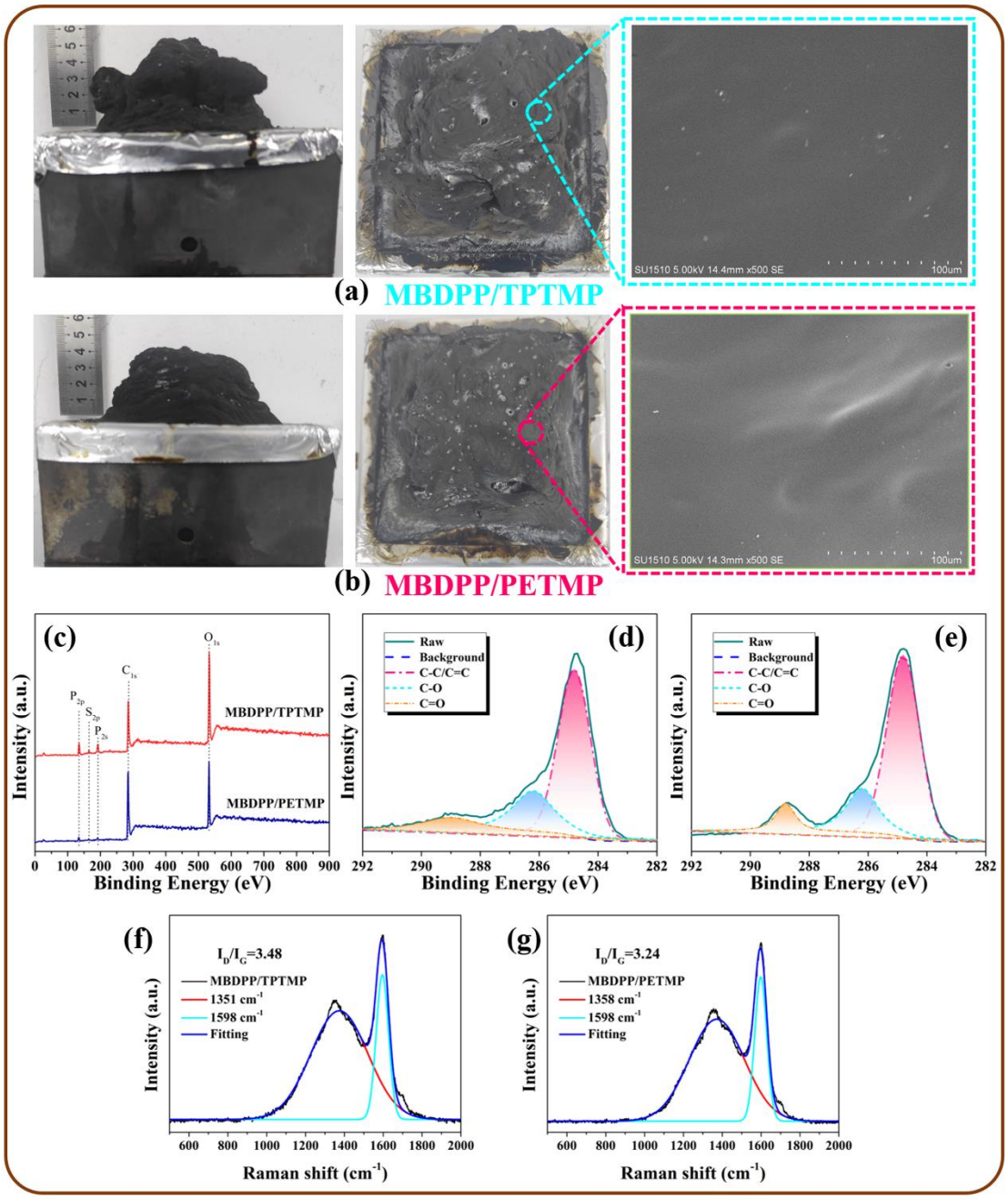

Fig. 7. Photographs and SEM images of the char residues of (a) MBDPP/TPTMP and (b) MBDPP/PETMP membranes after the cone calorimeter measurement; (c) The full-scan XPS spectra of the char residues of MBDPP/TPTMP and MBDPP/PETMP membranes; The high-resolution C1s XPS spectra of the char residues of (d) MBDPP/TPTMP and (e) MBDPP/PETMP membranes.

The elemental compositions of the char residues of MBDPP/TPTMP and MBDPP/PETMP membranes were investigated by XPS. Fig. 7c shows the full-scan XPS spectra of the char residues of MBDPP/TPTMP and MBDPP/PETMP membranes. Both the char residues of MBDPP/TPTMP and MBDPP/PETMP membranes exhibited several characteristic peaks including C_{1s} (284.74 eV), O_{1s} (532.86 eV), S_{2p} (163.99 eV), P_{2s} (192.48 eV) and P_{2p} (134.42 eV), which accorded well with the elemental compositions of MBDPP/TPTMP and MBDPP/PETMP membranes before combustion. Table S2 summarizes the atomic percentage of each element in the char residues. It can be found that the C/O ratio was 1.33 and 2.70 for the char residues of MBDPP/TPTMP and MBDPP/PETMP membranes, respectively, which implied the char residues of MBDPP/PETMP membrane had better thermal resistance. That was why MBDPP/PETMP membrane showed higher char yield in the TGA test. The high-resolution C1s XPS spectra of the char residues of MBDPP/TPTMP and MBDPP/PETMP membranes are provided in Fig. 7d and 7e, and the corresponding data are listed in Table S3. The high-resolution C1s XPS peak of both the samples could be deconvoluted into three sub-peaks at 284.8, 286.2 and 289.0 eV, which were ascribed to C-C/C=C, C-O and C=O, respectively[36-40]. The ratio between unoxidized carbon atoms (C-C/C=C) and oxidized ones (C-O and C=O) is generally utilized to assess the thermal oxidative resistant behavior of carbonaceous materials [41, 42]. The ratio between unoxidized carbon atoms and oxidized ones was calculated to be 1.57 and 2.20 for the char residues of MBDPP/TPTMP and MBDPP/PETMP membranes, respectively, which also indicated the better thermal resistance of the char residues of

MBDPP/PETMP membrane.

The graphitization degree of char residues after combustion was also utilized to evaluated the fire safety of polymeric materials[43]. Raman spectroscopy was performed to further observe the graphitization degree of MBDPP/TPTMP and MBDPP/PETMP membranes. As shown in Fig. 7f and 7g, the Raman spectrum of MBDPP/TPTMP and MBDPP/PETMP membranes likely presented two special bonds located at 1351 cm^{-1} (D bands) and 1598 cm^{-1} (G bands). The graphitization degree was obtained from the intensity ratio of D to G band (I_D/I_G), and lower I_D/I_G value indicates higher graphitization degree, and higher thermal and flame retardancy as well[44, 45]. The I_D/I_G values of MBDPP/TPTMP and MBDPP/PETMP were 3.48 and 3.24, respectively. It seems that MBDPP/PETMP possessed a lower I_D/I_G value, implying better shielding effect and condensed phase flame-retardant effect.

Based on the above analyses of thermal degradation and combustion behaviors as well as the condensed phase of the flame retardant MBDPP/TPTMP and MBDPP/PETMP membranes, a possible flame-retardant mechanism is proposed (as shown in Scheme 2). Once exposed to heat or flame, the MBDPP segment in the skeleton of MBDPP/TPTMP or MBDPP/PETMP matrix would firstly decompose to form phosphoric acid or polyphosphoric acids, which plays better catalytic effect on promoting the dehydration of the membrane matrix to form a stable carbonaceous char layer on the surface of the membranes. During combustion process, the formed char layer could act as a physical barrier which not only protect the inside membrane from attacks of outside flame and heat, but also restrain the volatile flammable gases

including aromatic compounds and hydrocarbon, etc. escape from the membrane to the flame zone to feed the combustion, and isolate oxygen as well. Hence, the thermally stable char layers could block the heat and mass transfer between outside flame zone and underlying substrate, resulting in the improvement of fire safety.

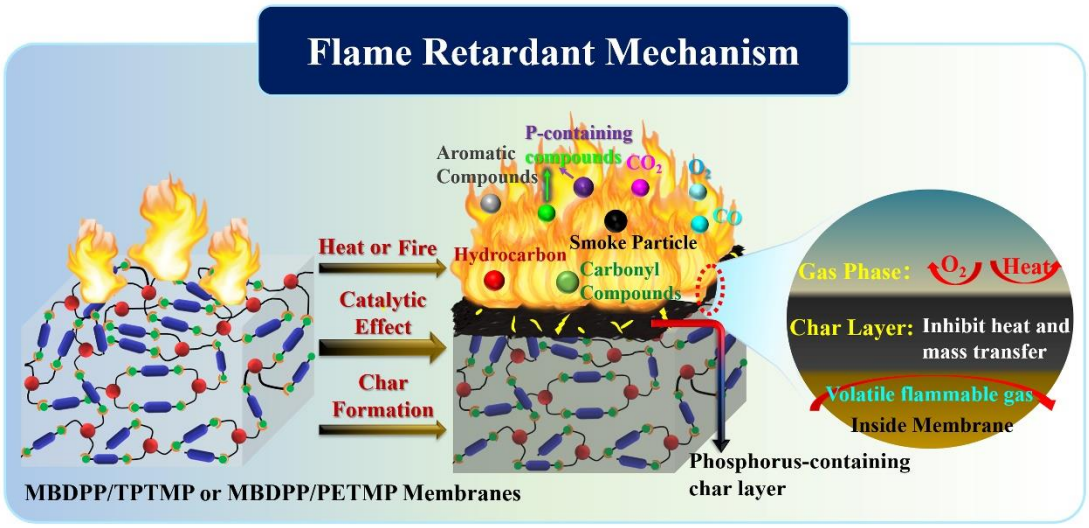

Scheme 2. The flame retardant mechanism of MBDPP/TPTMP and MBDPP/PETMP polymer films

4. Conclusion

In summary, a magnolol-derived bis(diphenyl phosphate) (MBDPP) monomer was successfully synthesized and characterized, and subsequently photo-cured with tri-thiol (TPTMP) or tetra-thiol (PETMP) monomers via thiol–ene polymerization. DMA results demonstrated that MBDPP/PETMP behaved higher storage modulus and T_g than MBDPP/TPTMP owing to the higher cross-linking density of the former system. TGA results manifested that MBDPP/TPTMP and MBDPP/PETMP membranes possessed excellent charring capacity under both air and nitrogen atmospheres. MBDPP/TPTMP and MBDPP/PETMP membranes presented exceptional intrinsic anti-flammability, as

evidenced by the open flame test and the cone calorimeter measurement. These membranes were prone to form an intact, dense and expanded carbonaceous layer during combustion, and this carbonaceous layer could serve as an effective barrier for flammable pyrolysis products and heat irradiation, thus accounting for the exceptional intrinsic anti-flammability. In addition, MBDPP/TPTMP and MBDPP/PETMP membranes also possessed good flexibility and high transparency. These fascinating comprehensive properties make these bio-based membranes promising candidates for intumescent flame retardant and transparent coating application.

Acknowledgements

We gratefully acknowledge financial support from the Textile Light Applied Basic Research Project (Grant No.: J202107), the Hong Kong Scholars Program (Grant No.: XJ2020003), the Doctor Project of Innovation and Entrepreneurship in Jiangsu Province (Grant No.: JSSCBS20210821) and the Basic Research Program of Jiangnan University (Grant No.: JUSRP121029).

References

[1] Liu F, Liu A, Tao W, Yang Y. Preparation of UV curable organic/inorganic hybrid coatings-a review. Prog Org Coat. 2020;145:105685.

[2] Mendes-Felipe C, Oliveira J, Etxebarria I, Vilas-Vilela JL, Lanceros-Mendez S. State-of-the-Art and Future Challenges of UV Curable Polymer-Based Smart Materials for Printing Technologies. Advanced Materials Technologies. 2019;4(3):1800618.

[3] Chen XL, Hu Y, Jiao CM, Song L. Preparation and thermal properties of a novel flame-retardant coating. Polym Degrad Stabil. 2007;92(6):1141-50.

[4] Liang H, Shi WF. Thermal behaviour and degradation mechanism of phosphate di/triacrylate used for UV curable flame-retardant coatings. Polym Degrad Stabil. 2004;84(3):525-32.

[5] Cheng XE, Shi WF. UV-curing behavior and properties of tri/di(acryloyloxyethyloxy) phenyl silane used for flame-retardant coatings. Prog Org Coat. 2010;69(3):252-9.

[6] Hoyle CE, Bowman CN. Thiol–Ene Click Chemistry. Angewandte Chemie International Edition. 2010;49(9):1540-73.

[7] Lee TY, Guymon CA, Jönsson ES, Hoyle CE. The effect of monomer structure on oxygen inhibition of (meth)acrylates photopolymerization. Polymer. 2004;45(18):6155-62.

[8] Liu C, Li T, Zhang J, Chen S, Xu Z, Zhang A, et al. Preparation and properties of phosphorous–nitrogen containing UV-curable polymeric coatings based on thiol–ene click reaction. Prog Org Coat. 2016;90:21-7.

[9] Çakmakçı E, Mülazim Y, Kahraman MV, Apohan NK. Preparation and characterization of boron containing thiol–ene photocured hybrid coatings. Prog Org Coat. 2012;75(1):28-32.

[10] Çakmakçı E, Mülazim Y, Kahraman MV, Apohan NK. Flame retardant thiol–ene photocured coatings. Reactive and Functional Polymers. 2011;71(1):36-41.

[11] Baştürk E, Oktay B, Kahraman MV, Kayaman Apohan N. UV cured thiol-ene flame retardant hybrid coatings. Prog Org Coat. 2013;76(6):936-43.

[12] Wang T, Li L, Wang Q, Xie G, Guo C. Castor oil based UV-cured coatings using

thiol-ene click reaction for thermal degradation with flame retardance. Industrial Crops and Products. 2019;141:111798.

[13] Wang T, Li L, Cao Y, Wang Q, Guo C. Preparation and flame retardancy of castor oil based UV-cured flame retardant coating containing P/Si/S on wood surface. Industrial Crops and Products. 2019;130:562-70.

[14] Liu T, Sun LC, Ou RX, Fan Q, Li LP, Guo CG, et al. Flame retardant eugenol-based thiol-ene polymer networks with high mechanical strength and transparency. Chem Eng J. 2019;368:359-68.

[15] Guo W, Wang X, Huang J, Mu X, Cai W, Song L, et al. Phosphorylated cardanol-formaldehyde oligomers as flame-retardant and toughening agents for epoxy thermosets. Chem Eng J. 2021;423:130192.

[16] Cramer NB, Bowman CN. Kinetics of thiol-ene and thiol-acrylate photopolymerizations with real-time Fourier transform infrared. J Polym Sci Pol Chem. 2001;39(19):3311-9.

[17] Ranganathan T, Beaulieu M, Zilberman J, Smith KD, Westmoreland PR, Farris RJ, et al. Thermal degradation of deoxybenzoin polymers studied by pyrolysis-gas chromatography/mass spectrometry. Polymer Degradation and Stability. 2008;93(6):1059-66.

[18] Shabzendedar S, Modarresi-Alam AR, Bahrpeyma A, Noroozifar M, Kerman K. Novel conductive multi-walled polymeric nanotubes of poly (diazoaminobenzene) for single-layer polymer solar cell. Reactive and Functional Polymers. 2020;149:104529.

[19] Nabipour H, Wang X, Song L, Hu Y. A high performance fully bio-based epoxy

thermoset from a syringaldehyde-derived epoxy monomer cured by furan-derived amine. Green Chemistry. 2021;23(1):501-10.

[20] Nabipour H, Qiu S, Wang X, Song L, Hu Y. Phosphorus-Free Ellagic Acid-Derived Epoxy Thermosets with Intrinsic Antiflammability and High Glass Transition Temperature. Acs Sustain Chem Eng. 2021;9(32):10799-808.

[21] Cramer NB, Reddy SK, Cole M, Hoyle C, Bowman CN. Initiation and kinetics of thiol-ene photopolymerizations without photoinitiators. J Polym Sci Pol Chem. 2004;42(22):5817-26.

[22] Niu H, Nabipour H, Wang X, Song L, Hu Y. Phosphorus-Free Vanillin-Derived Intrinsically Flame-Retardant Epoxy Thermoset with Extremely Low Heat Release Rate and Smoke Emission. Acs Sustain Chem Eng. 2021;9(15):5268-77.

[23] Zhou X, Qiu S, Cai W, Liu L, Hou Y, Wang W, et al. Construction of hierarchical MoS2@TiO2 structure for the high performance bimaleimide system with excellent fire safety and mechanical properties. Chem Eng J. 2019;369:451-62.

[24] Ding H, Qiu S, Wang X, Song L, Hu Y. Highly flame retardant, low thermally conducting, and hydrophobic phytic acid-guanazole-cellulose nanofiber composite foams. Cellulose. 2021;28(15):9769-83.

[25] Ma Z, Liu X, Xu X, Liu L, Yu B, Maluk C, et al. Bioinspired, highly adhesive, nanostructured polymeric coatings for superhydrophobic fire-extinguishing thermal insulation foam. Acs Nano. 2021;15(7):11667-80.

[26] Lu J, Liao C, Cheng L, Jia P, Yin Z, Song L, et al. Cleaner production to a multifunctional polyurethane sponge with high fire safety and low toxicity release.

Journal of Cleaner Production. 2021:130172.

[27] Cao C-F, Yu B, Chen Z-Y, Qu Y-X, Li Y-T, Shi Y-Q, et al. Fire Intumescent, High-Temperature Resistant, Mechanically Flexible Graphene Oxide Network for Exceptional Fire Shielding and Ultra-Fast Fire Warning. Nano-Micro Letters. 2022;14(1):1-18.

[28] Bao X, Wu F, Wang J. Effect of a Reactive-Type Flame Retardant on Thermal Stability of Thiol-ene Composites. Journal of Macromolecular Science, Part B. 2021:1-9.

[29] Jiang S, Shi Y, Qian X, Zhou K, Xu H, Lo S, et al. Synthesis of a Novel Phosphorus- and Nitrogen-Containing Acrylate and Its Performance as an Intumescent Flame Retardant for Epoxy Acrylate. Ind Eng Chem Res. 2013;52(49):17442-50.

[30] Zhu SW, Shi WF. Combustion behaviour and thermal properties of UV cured methacrylated phosphate/epoxy acrylate blends. Polym Degrad Stabil. 2003;81(2):233-7.

[31] Zheng T, Ni X. Loading an organophosphorous flame retardant into halloysite nanotubes for modifying UV-curable epoxy resin. Rsc Adv. 2016;6(62):57122-30.

[32] Tao Y, Liu C, Li P, Wang B, Xu Y-J, Jiang Z-M, et al. A flame-retardant PET fabric coating: Flammability, anti-dripping properties, and flame-retardant mechanism. Progress in Organic Coatings. 2021;150:105971.

[33] Xie W, Han Z, Zhang Z, Liu Y, Wang Q. Hydrogen bond complexasion to prepare guanidine phosphate flame retardant poly (vinyl alcohol) membrane with high transparency. Composites Part B: Engineering. 2019;176:107265.

[34] Liu C, Li P, Xu Y-J, Liu Y, Zhu P, Wang Y-Z. Epoxy/iron alginate composites with improved fire resistance, smoke suppression and mechanical properties. Journal of Materials Science. 2022:1-17.

[35] Sui Y, Sima H, Shao W, Zhang C. Novel bioderived cross-linked polyphosphazene microspheres decorated with FeCo-layered double hydroxide as an all-in-one intumescent flame retardant for epoxy resin. Composites Part B: Engineering. 2022;229:109463.

[36] Stankovich S, Dikin DA, Piner RD, Kohlhaas KA, Kleinhammes A, Jia Y, et al. Synthesis of graphene-based nanosheets via chemical reduction of exfoliated graphite oxide. Carbon. 2007;45(7):1558-65.

[37] Wang X, Song L, Yang HY, Xing WY, Kandola B, Hua Y. Simultaneous reduction and surface functionalization of graphene oxide with POSS for reducing fire hazards in epoxy composites. J Mater Chem. 2012;22(41):22037-43.

[38] Mu X, Zhou X, Wang W, Xiao Y, Liao C, Longfei H, et al. Design of compressible flame retardant grafted porous organic polymer based separator with high fire safety and good electrochemical properties. Chem Eng J. 2021;405:126946.

[39] Liao C, Hou Y, Han L, Zhu Y, Wang H, Wu N, et al. Expandable nitrogen-doped carbon-based anodes fabricated from self-sacrificial metal-organic frameworks for ultralong-life lithium storage. Carbon. 2022;186:46-54.

[40] Cao C-F, Yu B, Guo B-F, Hu W-J, Sun F-N, Zhang Z-H, et al. Bio-inspired, sustainable and mechanically robust graphene oxide-based hybrid networks for efficient fire protection and warning. Chemical Engineering Journal. 2022:134516.

[41] Bourbigot S, LeBras M, Delobel R, Gengembre L. XPS study of an intumescent coating .2. Application to the ammonium polyphosphate pentaerythritol ethylenic terpolymer fire retardant system with and without synergistic agent. Appl Surf Sci. 1997;120(1-2):15-29.

[42] Wang X, Zhou S, Xing W, Yu B, Feng X, Song L, et al. Self-assembly of Ni-Fe layered double hydroxide/graphene hybrids for reducing fire hazard in epoxy composites. J Mater Chem A. 2013;1(13):4383-90.

[43] Yang J, Zhang A, Chen Y, Wang L, Li M, Yang H, et al. Surface modification of core–shell structured ZIF-67@ Cobalt coordination compound to improve the fire safety of biomass aerogel insulation materials. Chemical Engineering Journal. 2022;430:132809.

[44] Hou Y, Liao C, Qiu S, Xu Z, Mu X, Gui Z, et al. Preparation of soybean root-like CNTs/bimetallic oxides hybrid to enhance fire safety and mechanical performance of thermoplastic polyurethane. Chemical Engineering Journal. 2022;428:132338.

[45] Hou Y, Qiu S, Xu Z, Chu F, Liao C, Gui Z, et al. Which part of metal-organic frameworks affects polymers' heat release, smoke emission and CO production behaviors more significantly, metallic component or organic ligand? Composites Part B: Engineering. 2021;223:109131.